Rapid NEGF-Based Calculation of Ballistic Current in Ultra-Short DG MOSFETs for Circuit Simulation

Fabian Hosenfeld, Fabian Horst, Michael Graef, Atieh Farokhnejad,
Alexander Kloes, Benjamín Iñíguez, and François Lime

***Abstract*—Shrinking gate length in conventional MOSFETs leads to increasing short channel effects like source-to-drain (SD) tunneling. Compact modeling designers are challenged to model these quantum mechanical effects. The complexity lies in the set-up between time efficiency, physical model relation and analytical equations. Multi-scale simulation bridges the gap between compact models, its fast and efficient calculation of the device terminal voltages, and numerical device models which consider the effects of nanoscale devices. These numerical models iterate between Poisson- and Schroedinger equation which significantly slows down the simulation performance. The physics-based consideration of quantum effects like the SD tunneling makes the non-equilibrium Green's function (NEGF) to a state-of-the-art method for the simulation of devices in the sub 10 nm region.**

This work introduces a semi-analytical NEGF model for ultra-short DG MOSFETs. Applying the closed-form potential solution of a classical compact model, the model turns the NEGF from an iterative numerical solution into a straightforward calculation. The applied mathematical approximations speed up the calculation time of the 1D NEGF. The model results for the ballistic channel current in DG-MOSFETs are compared with numerical NanoMOS TCAD [1] simulation data. Shown is the accurate potential calculation as well as the good agreement of the current characteristic for temperatures down to 75 K for channel lengths from 6 nm to 20 nm and channel thickness from 1.5 nm to 3 nm.

***Index Terms*—Ultra-Short Double-Gate (DG) MOSFET, Non Equilibrium Green's Function (NEGF), Ballistic Transport, Source-to-Drain (SD) Tunneling, Ultra-Thin Body (UTB), Compact Model, Multiscale Simulation.**

I. Introduction

NOWADAYS, the MOSFET is the most technologically advanced device of the transistor variety. During its scaling process, the investigated channel length gets down below 10 nm. Due to the source-to-drain (SD) tunneling effects, this characteristic length is physically limited (see Fig.1) [2], [3], [4]. Overcoming this geometry milestone of 10 nm is always resulting in a significant increase of the device's OFF-current, hence reducing the on/off ratio and a degradation of the subthreshold slope (S). Based on the non-equilibrium Green's function (NEGF) formalism introduced by Keldysh, Kadanoff and Baym, the quantum mechanical and SD tunneling effects are inherently considered [2], [3], [4], [5]. Therefore, the formalism has become one of the most promising current calculation methods for TCAD simulations [1], [6], [7], [8]. In order to transfer these mathematics from numerical device simulations to numerically efficient compact transistor models for circuit simulation, a reduction from many numeric steps to a few calculations is necessary (see Fig. 2).

This work is based on the DG MOSFET shown in Figure 3. Its source and drain regions are highly n-doped and the channel stays intrinsic, whereby an ideal doping profile is assumed. For an increased influence on the channel region, the gate dielectric consists of a high-κ oxide material with the dielectric constant $\epsilon_{ox} = 25 \cdot \epsilon_0$. For a channel thickness down to $t_{ch} = 1.5\,\mathrm{nm}$ and a channel length down to $l_{ch} = 6\,\mathrm{nm}$ a fully ballistic current transport in the channel is assumed.

First results have been presented in [9], in this paper the approach is more detailed and less fitting parameters are used.

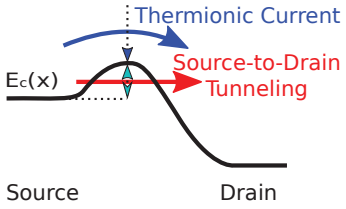

Figure 1. Thermionic current and SD tunneling current of a short channel transistor [3].

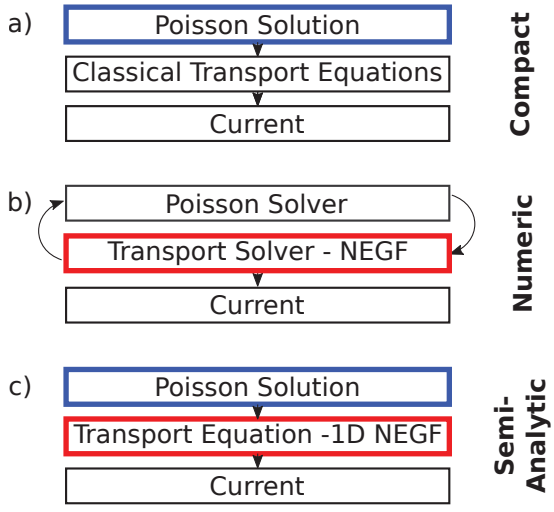

Figure 2. Flowchart of a) standard compact models using analytical solved equations, b) common numerical NEGF models which iterate between transport and Poisson solver c) new semi-analytic NEGF model without iterations.

II. Non-Iterative NEGF Current Model

Following, the derivation of the semi-analytical DG MOSFET model is introduced. State-of-the-art compact models (see

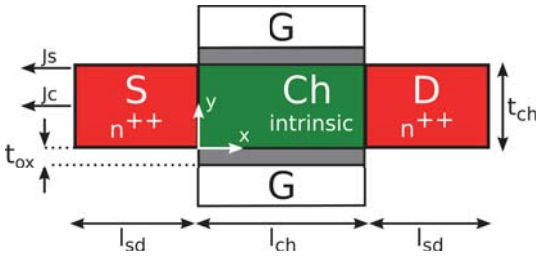

Figure 3. Geometry of a DG MOSFET showing the doping profiles, structural parameters and the 1D current density at specific y-positions: J_s at the surface and J_c at the center.

Fig. 2(a)) use classical transport equations. These transport equations are only able to calculate the tunneling current by introducing approximations or using empirical equations. On the other hand, the NEGF calculates the thermionic emission current and the tunneling current based on physical equations. Coupling the NEGF with Poisson's equation leads to self-consistent results but increase the simulation time (see Fig. 2(b)). For the semi-analytical model, the time consuming iterative coupling of Poisson's equation with the NEGF solver is omitted. As depicted in Fig. 2(c), the approach consists of three main parts which distinguish this model from other models. In the first part of the semi-analytical model, the accurate calculation of the device potential is done. In a first step, the focus is on the subthreshold region of the device. Therefore, the mobile charges can be neglected in the solution of Poisson's equation. The effect of mobile charges on the device electrostatics need to be incorporated in a further step. Based on the accurate potential calculation the conduction band structure is calculated for certain geometry- and material variations. The band structure together with the effective mass Hamiltonian are important input parameters to formulate the Green's function. Together with the Fermi level of each contact, the electron density and hence the current density for a specific energy level is calculated.

The fast and efficient drain current calculation is done by an interpolation between some specific and significant energy levels. The accuracy of this not self-consistent model is validated by comparing with self-consistent numerical device simulations in section IV.

A. Electrostatics

The closed-form potential solution is based on an analytical model for Double-Gate Tunnel-FETs published in [10]. Aiming for a precise potential of the device, the Poisson equation needs to be solved. Because solving the Laplace equation is much more convenient for compact models and almost accurate in subthreshold region, the mobile charges are neglected in a first step:

$$\Delta\Phi_{2D} = -\frac{\rho}{\epsilon} \quad \rightarrow \quad \Delta\Phi_{2D} \approx 0. \tag{1}$$

Mobile Charges

So far, the Laplace solution is only accurate in the subthreshold region. In order to take respect to the mobile charges, these charges are estimated in a closed-form approach obtained from [11]. The inversion charge is $Q'_{i,s}$ calculated by:

$$Q'_{i,s} = 2\alpha C'_{ox} V_{th} \times \mathcal{L}\left\{\frac{Q'_{i,0}}{2\alpha C'_{ox} V_{th}} \times \exp\left(\frac{2C'_{ox}(V_{gs}-V_0)+Q'_{i,0}}{2\alpha C'_{ox} V_{th}}\right)\right\}. \tag{2}$$

Here, $Q'_{i,0}$ is the mobile electron charge at an arbitrary gate bias $V_{gs} = V_0$, which in this model is set to the flatband voltage, $V_0 = V_{fb}$:

$$Q'_{i,0} = q \cdot n_i \cdot t_{ch}. \tag{3}$$

V_{th} is the thermal voltage, C'_{ox} the capacitance per gate area, and $\mathcal{L}$ is the first branch of Lambert's W-function. The subthreshold slope degradation is calculated by the parameter α, which would be 1 for an ideal subthreshold slope of $60\frac{mV}{dec}$. The effect of the mobile charges on the potential is largest at the barrier, whereas it becomes negligible for increasing distance along the x-axis. Therefore, the resulting inversion layer $\frac{Q'_{i,s}}{2}$ of the channels surface is calculated by assuming a constant charge density along the channel. Especially for pure ballistic transport, this assumption fits well, because the mobile charges are not able to change their energy level. This behavior leads to an constant current in x-direction at each energy level. Hence, the inversion charge shields a part of the gate voltage, whereas only a reduced gate voltage influences the channel region:

$$V'_g = V_g - \left(\frac{Q'_{i,s}}{2 \cdot C_{ox}}\right). \tag{4}$$

This method leads to an almost constant barrier height in the above threshold region. In the following potential equation, this reduced gate bias V'_g is used as a boundary condition along the gate electrode as well for the calculation of the long channel surface potential in Eq. (7).

Boundary conditions

The potential within the channel is calculated by the surrounding boundary conditions shown in Fig. 4. The applied boundary conditions are the gate potential Eq. (4) and the effective built-in potential Eq. (5) which describes the potential at the source and drain to channel junctions.

In the following equations the calculation of the effective built-in potential is introduced:

$$\Phi_{bi,eff,s/d} = \Phi_{bi,s/d} \pm \Delta\Phi_{bi,s/d}, \tag{5}$$

with the built-in potential in source and drain region $\Phi_{bi,s/d}$. Whereby $\Delta\Phi_{bi,s/d}$ is calculated by [10]:

$$\Delta\Phi_{bi,s/d} = \Phi_{bi,s/d} + V_{s/d} - \Phi_{sp} + \lambda^2 \cdot \frac{q}{\epsilon_{si}} \cdot N_D \times \left[1 - \sqrt{1 + \frac{2(\Phi_{bi,s/d}+V_{s/d}-\Phi_{sp})}{\lambda^2 \frac{q}{\epsilon_{si}} N_D}}\right], \tag{6}$$

with the donor doping concentration N_D, silicon permittivity ϵ_{si}, drain and source potential $V_{s/d}$, screening length λ. The long channel surface potential Φ_{sp} is the potential at the channel to oxide junction:

$$\Phi_{sp} = V_g - V_{fb}. \tag{7}$$

Whereby the flatband voltage V_{fb} is adopted to the TCAD results.

Strategy of Decomposing

The first component consists of a closed-form solution of the 2D Laplace equation in the 4-corner channel region. As shown in Fig. 4(a) the potential at the junctions consists of an mixture of constant and parabolic shaped potentials.

Decomposing this four corner structure of the channel into two separate two-corner structures, source related case of the channel and drain related case of the channel, leads to a much simpler calculation of the electrostatic channel potential.

In a next step, the mixed boundary conditions are separated into both cases, the case of constant boundary conditions (see Fig. 4(b), 4(d)) and the parabolic shaped (see Fig. 4(c), 4(e)). Finally, the decomposing leads to four separate two-corner structures.

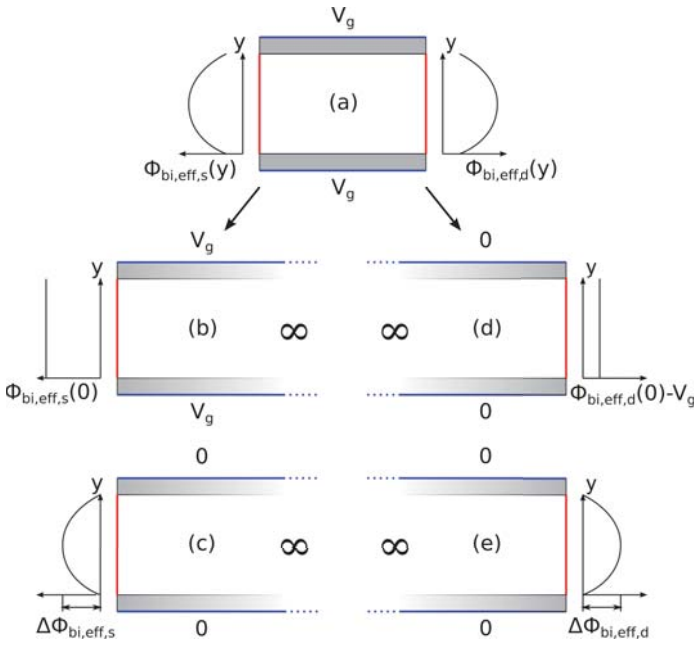

Figure 4. Decomposition of the boundary conditions of a DG MOSFET. (a) Boundary conditions of the whole device with parabolically shaped potentials at the channel junctions. (b) source- (d) drain-related case conditions with constant boundary for 2D Laplace solution. (c) source- (e) drain-related case conditions for 2D solution with parabolic boundaries at the channel junctions [10].

Conformal Mapping

The conformal mapping technique, or more specifically the Schwarz-Christoffel transformation is applied to map the device and its boundary conditions depending on x and y into the upper half of a complex w-plane depending on u and v [12]:

$$w = u + jv = \cosh\left(\frac{\pi(x+jy)}{\Delta y}\right). \tag{8}$$

Laplace Equation

The Laplace equation within the mapped w-plane is given by [13]:

$$\varphi(u,v) = \frac{1}{\pi}\int_{-\infty}^{\infty} \frac{v}{(u-\bar{u})^2+v^2} \cdot \varphi(\bar{u}) \cdot d\bar{u}, \tag{9}$$

with $\varphi(\bar{u})$ as the mapped boundary conditions along the device geometry. In a further step, source and drain potential extensions are calculated and connected with the channel potential. At the end a set of closed-form analytical equations for the potential in the device cross-section is obtained [10].

B. Link Between Electrostatics and NEGF

Because the NEGF is a very time consuming calculation method and each dimension dramatically increases the calculation effort, a one dimensional NEGF is implemented. Therefore, one dimensional slices of the conduction band in x-direction $E_c(x)$ need to be extracted out of the 2D potential solution (Fig. 1). Within the NEGF, each slice of the conduction band is treated to be independent. Using more slices, produces higher accuracy for the 2D device behavior, on the other hand using less slices gives higher speed. In this case, there are only two slices extracted out of the 2D profile. One at the channel surface $E_{c,s}(x)$ and the other at the channel center $E_{c,c}(x)$ (see Fig. 6a). Applying the 1D NEGF, $E_{c,s}(x)$ leads to J_s and $E_{c,c}(x)$ leads to J_c, respectively (see Fig. 3).

C. Quantum Confinement

Quantum confinement is an quantum mechanical effect which influences heavily the behavior of transistors. It plays an important role for ultra-thin transistors with a channel thickness below 4 nm. This effect is mainly implemented in compact models by an adoption of the threshold voltage [14] as well as the flatband voltage [15]. Common NEGF based TCAD simulators considers this 2 dimensional effect by solving Schroedinger's equation in the confinement direction. The 1D model needs to do it in a compact way and includes this quantum effect by an addition of the energy ΔE to the physical value of the flatband voltage:

$$V_{fb} = V_{fb,phy} + \Delta E. \tag{10}$$

This energy change caused by the confinement within the channel caused by the small channel thickness t_{ch} is given by [11]:

$$\Delta E = \frac{\hbar^2 \pi 2}{2 m_e t_{ch}^2}. \tag{11}$$

D. Current Calculation

Supriyo Datta presented in [5] and [16] a self-consistent 1D NEGF method for considering quantum current transport in highly doped resistors. Turning this method into a straightforward calculation makes the algorithm much faster and also suitable for this compact transistor model. A fundamental description of the Green's function is given by [17], [18], [19]. The movement of the electrons within the parabolic conduction

band of the semiconductor is described by the effective mass Hamiltonian $H = -(\hbar^2/2m)\nabla^2)$. The longitudinal part of the Hamiltonian is given by:

$$H_L = E_c - \frac{\hbar^2 d^2}{2mdx^2} + U(x), \tag{12}$$

with E_c as the physical conduction band energy of doped silicon. The 1D energy profile of the conduction band, calculated by the potential solution from Section II-B at the discrete positions inside the device, is used as $U(x)$ in Eq. (12). Applying for the longitudinal Hamiltonian, a discrete lattice in real space results in the Hamiltonian matrix H_L. The finite difference method is used to approximate the second order derivative of Eq. (12) in Matrix form:

$$H_L = \begin{bmatrix} E_c{+}2t{+}U(1) & -t & \cdots & 0 \\ -t & E_c{+}2t{+}U(2) & \cdots & 0 \\ \vdots & \vdots & \ddots & \vdots \\ 0 & 0 & \cdots & -t \\ 0 & 0 & \cdots & E_c{+}2t{+}U(N) \end{bmatrix} \tag{13}$$

with the Hamiltonian $t = \hbar^2/2ma^2$ and a as the grid size. The self-energy functions Σ_1 and Σ_2 describe the connection of the device to the semi infinite contacts, using open boundary conditions. Both functions treat the device to just have outgoing waves at the ends. $\Sigma_{1,2}$ depend on the energy and are not hermitian, like the Hamiltonian matrix. The self-energy terms change the Hamiltonian from H_L to $\hat{H}_L$, which have an effect on their energies and eigenstates. Secondly, the self-energy terms add an imaginary energy part to the broadening functions $[\Gamma_1]$ and $[\Gamma_2]$:

$$\Sigma_1 = \begin{bmatrix} -t\exp(ik_1a) & 0 & \cdots & 0 \\ 0 & 0 & \cdots & 0 \\ \vdots & \vdots & \ddots & \vdots \\ 0 & 0 & \cdots & 0 \end{bmatrix}, \tag{14}$$

where (k_1a) is calculated with the help of the following equation:

$$E = E_c + U(1) + 2t(1 - \cos(k_1a)), \tag{15}$$

whereby E is the considered energy level. The $\Gamma_{1,2}$ functions broaden the energy level due to the connections of the device with the leads. An electron initially placed in that state will escape into the left and right leads with the time constant $\hbar/\gamma$. Whereby γ denotes one element of the $\Gamma_{1,2}$ matrix:

$$\Gamma_1 = i\left[\Sigma_1 - \Sigma_1^+\right], \qquad \Gamma_2 = i\left[\Sigma_2 - \Sigma_2^+\right]. \tag{16}$$

The energy level is broaden from a delta-function $\delta(E - \epsilon)$ into a line of a shape that does not have to be Lorentzian. The retarded Green's function $[G]$ represents the device's system response to an input stimulus. It consists of a matrix subtraction of the considered energy level E, the Hamiltonian matrix $[H_L]$ and the self-energy functions of each contact $[\Sigma_1]$ and $[\Sigma_2]$:

$$G(E) = \left[EI - H_L - \Sigma_1 - \Sigma_2\right]^{-1}, \tag{17}$$

whereby I constitutes the identity matrix. Due to the discrete lattice with about 100×100 matrices, the inversion of the matrix is a time consuming part of the model. In the next step, the formalism separates the spectral function $[A]$ into the source $[A_1]$ and the drain $[A_2]$ spectral function. Both are formulated out of the Green's function multiplying with the Γ of each contact:

$$A_1 = G\Gamma_1 G^+, \qquad A_2 = G\Gamma_2 G^+. \tag{18}$$

Filling up the spectral function $[A]$, which could also be seen as the available density of states, according to the Fermi function of each contact F_1 and F_2, leads to the electron density matrix $[\tilde{\rho}(E)]$ of a considered energy level E:

$$[\tilde{\rho}(E)] = \frac{F_1[A_1(E)] + F_2[A_2(E)]}{2\pi}. \tag{19}$$

Regarding to the high doping of the source and drain regions, the semiconductor is degenerated and the Boltzmann statistics needs to be replaced by the Fermi distribution. The Fermi function is calculated for a 2D device structure described by the $\mathcal{F}_0$ distribution [20]:

$$n = N_c \cdot \mathcal{F}_0(\eta) \tag{20}$$

$$\mathcal{F}_0(\eta) = \int_0^\infty \frac{\xi^0}{1 + e^{\xi - \eta}} \mathrm{d}\xi, \tag{21}$$

$$\eta = \frac{E_f - E_c}{k_B \cdot T}. \tag{22}$$

where N_c is the effective density-of-states, and E_f the Fermi level which is adjusted to achieve a good current characteristic according to the ultra-thin channel thickness.

To calculate the current density in x-direction, the current operator $-(i\hbar mL)\delta/\delta x$ is presented in matrix form using the finite difference representation as:

$$[J_{op}] = (t/\hbar N) \begin{bmatrix} 0 & -j & 0 & 0 & \cdots & 0 \\ +j & 0 & -j & 0 & \cdots & 0 \\ 0 & +j & 0 & -j & \cdots & \vdots \\ \vdots & \vdots & \vdots & \vdots & \ddots & -j \\ 0 & 0 & 0 & \cdots & +j & 0 \end{bmatrix}, \tag{23}$$

with N being the number of points on the lattice. The matrix multiplication of the density matrix $[\tilde{\rho}(E)]$ and the current operator $[J_{op}]$ leads to the current density $\tilde{J}(E, y, z)$ at the considered energy level E:

$$\tilde{J}(E, y, z) = -q \cdot Trace(\tilde{\rho}(E) J_{op}). \tag{24}$$

To get the total current density, equation (24) must be integrated over energy, which is computationally extensive, because all associated density matrices are needed:

$$J(y, z) = \int \tilde{J}(E, y, z) dE. \tag{25}$$

Furthermore, the total current density must also be integrated over the channel cross section to describe the two dimensional device behavior.

III. Approximations for Increased Numerical Efficiency

The calculation time of the model depends in a large part on the integration over energy for all current densities (Fig. 5). An reduction from hundreds to few calculations speeds up the total calculation time of the model by almost the same factor. Also the description of the multidimensional device behavior slows down the simulation speed.

A. Energy Dependent Approximation

In order to do so without losing much accuracy, the current density is only calculated at some distinctive energy levels, which represent significant points (see Fig. 5). In this case, the current density for the associated energy levels is approximated with $i = 4$ parabolic functions which are built out of $j = 9$ significant points. As it is shown in Fig. 5, the current density per energy in log-scale is almost parabolic or linear shaped. The interpolation parameters a, b, c of the quadratic functions in Eq. (26) are calculated using the log-scaled values of the calculated current density $log_{10}(\tilde{J}(E_i, y, z))$. In the next step, each parabolic function to the power of 10 is built matching three of the 9 significant points. In the last step, the current density integration for the parabolic functions is done by:

$$J_i(y,z) = \int_{E_j}^{E_{j+2}} (10^{a_i \cdot E^2 + b_i \cdot E + c_i})\, dE. \tag{26}$$

Summing up all four parts of the current density leads to the total 1D current density for all associated energies at one specific y,z-position in the channel cross section:

$$J(y,z) = \sum_{i=1}^{4} J_i(y,z). \tag{27}$$

To describe the behavior of the current density depending on energy in a good manner, the significant points have to be chosen carefully. The first distinctive point is located at the energy level of the source conduction band E_c. At this energy level the current from source to drain starts to flow. A further sampling point is located at the Fermi level E_{f1}. The next sampling point equals the height of the energy barrier E_b (see Fig. 5). In most cases the biggest current density is located at this energy level. For energies above the energy barrier, the current density decreases. To approximate this trend of the thermionic emission current at the top of the energy barrier, the current density is calculated at 3 additional energies above the barrier. To account for the SD tunneling current the other 4 sampling points are distributed between the source energy E_{f1} and the energy barrier E_b.

B. Geometry Dependent Approximation

Considering plenty of 1D current densities to describe the 3D device increases the calculation effort. The number of 1D current density calculations needs to be a minimum.

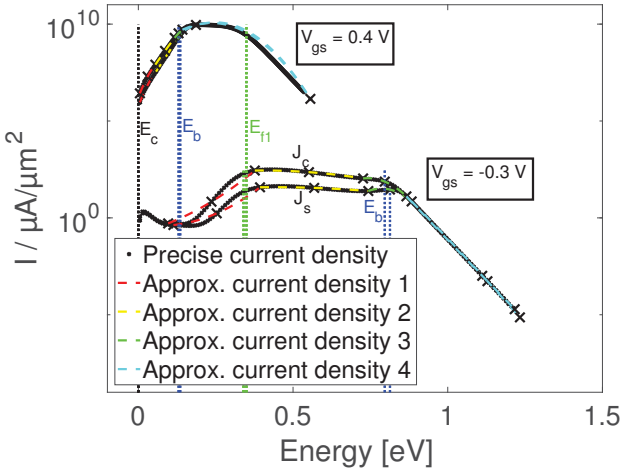

(a) Channel length $l_{ch} = 6\,\mathrm{nm}$.

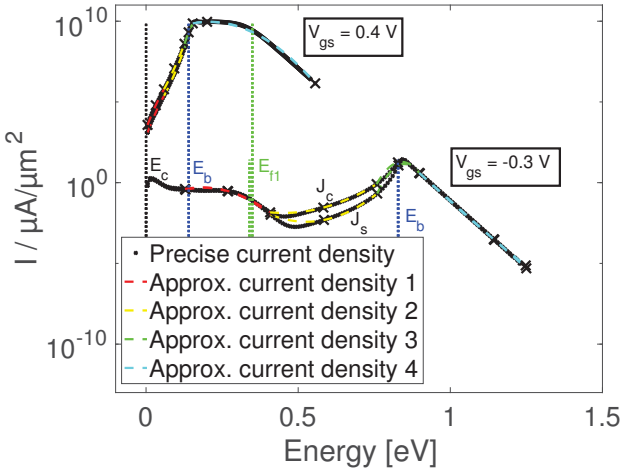

(b) Channel length $l_{ch} = 10\,\mathrm{nm}$.

Figure 5. Surface J_s and center J_c current density at the energy levels for $t_{ch} = 2\,\mathrm{nm}$ at $V_{ds} = 0.05\,\mathrm{V}$. The precise current density is calculated at each energy level by Eq. (24). The "Approx. current density" shows the current density as it is approximated by the mathematical functions of Eq. (26), which are defined by the current densities calculated only at positions marked by an "x". Additionally, the energy level of the conduction band E_c, the source Fermi level E_{f1} and the hight of the energy barrier E_b are shown. Considering the subthreshold region, in contrast to 10 nm channel length device, the current density at energies below the energy barrier of the 6 nm device is bigger and almost constant by reason of SD-tunneling.

Therefore, the current density $J(y,z)$ is calculated for only two slices, surface (current density J_s), and the other at the channel center (current density J_c) (see Fig 3). A closed-form integration using a parabolic function between both positions approximates the half of the device current I_d. Due to the symmetry of the device the drain current can be calculated by a multiplication with 2 and the device width W:

$$I_d = 2W \cdot \int_0^{\frac{t_{ch}}{2}} (a \cdot y^2 + b \cdot y + c)\, dy. \tag{28}$$

IV. Model Verification

The applied device parameters for the simulations are: $l_{sd} = 10\,\mathrm{nm}$, $t_{ox} = 1\,\mathrm{nm}$, $N_{sd} = 2 \cdot 10^{20}\,\mathrm{cm}^{-3}$, $\epsilon_{ox} = 25 \cdot \epsilon_0$, effective mass of carriers $m = 0.19 \cdot m_0$, the Fermi level $E_{f1,f2}$ as well as the effective density-of-states N_c is fitted for each channel thickness. The channel length and the channel thickness are individual for each simulation result and are mentioned in each figure. The accurate potential calculation of 6 nm channel length device is shown in Fig. 6(a). Especially for the tunneling current, the barrier length is very important. Fig. 6(b) illustrates the electron density for the associated energies in one 1D slice calculated by the model, which clearly shows interference in the band structure. Also it can be seen that the electron density within the energy barrier does not equals zero and hence shows SD tunneling.

The transfer characteristic of the $6, 8, 10, 20\,\mathrm{nm}$ channel length device for a channel thickness of $t_{ch} = 2\,nm$ is shown in Fig. 7(a). The figure highlights the SD tunneling effect, because the subthreshold slope gets worse for the device with a 6 nm channel length. The thermionic emission current is almost the same for a channel length of 10 nm and 20 nm through the ballistic current calculation. The strong influence of the small channel thickness on the threshold voltage can be seen in Fig. 7(b). The threshold voltage of the device is shifted because of the quantum confinement effect. The currents are shown for the 6 nm channel length device and for both channel thicknesses $t_{ch} = 1.5, 2\,nm$. The same influence is shown in Fig. 7(c), where the channel thickness is varied $t_{ch} = 1.5, 2, 3\,\mathrm{nm}$ by a channel length of $l_{ch} = 10\,nm$. Additionally, the slope of th 10 nm channel length devices is close to the ideal subthreshold slope of $60\,\frac{mV}{dec}$ caused by the good electrostatic control and less SD tunneling.

To highlight the SD-tunneling effects, the currents at a temperature of 300 K are compared to the currents at 75 K (see Fig. 8). For 75 K the thermionic current is repressed and the total current is dominated by the SD tunneling. Figure 8 also indicates the ideal slope of 15 mV / dec, which could be achieved at 75 K when only thermionic emission current occurs. Whereas, the simulation indicates a much worse slope, which is a result of the additional SD tunneling. The difference between 75 K and 300 K of the 6 nm device is small because the SD tunneling dominates in both cases. For the 10 nm device, the difference is increased, in consequence of less tunneling current.

The associated output characteristic at T=300 K for the 6 nm and 10 nm channel length device is given in Figure 9(a) and 9(b), respectively. The output as well as the transfer characteristics of the semi-analytical NEGF model stay in good agreement to the TCAD data.

V. Conclusion

In this work an semi-analytical approach for the calculation of the ballistic current in DG MOSFETs has been introduced. The model is based on a combination of a 2D analytical closed-form potential model and a compact non-numeric NEGF formalism. The model implementation is done in MATLAB and shows a good agreement with the TCAD simulation data for transistors with ultra-short channel lengths down to 6 nm and an ultra-thin body of 1.5 nm to 3 nm. The SD-tunneling is calculated in a good way and highlighted at low temperatures where the thermionic emission current is repressed. The model correctly predicts this effect, because it inherently includes thermionic emission and SD tunneling. A variation of channel length and thickness confirms a good scalability of the modeling approach. The analytic current calculation of the 3D device using 1D current densities at a few distinctive energies leads to a notable drop in calculation time. Applying a standard laptop computer for the calculation of the transfer characteristic shown in Fig. 7(a) which consists of 70 bias steps is done in less than 10 s.

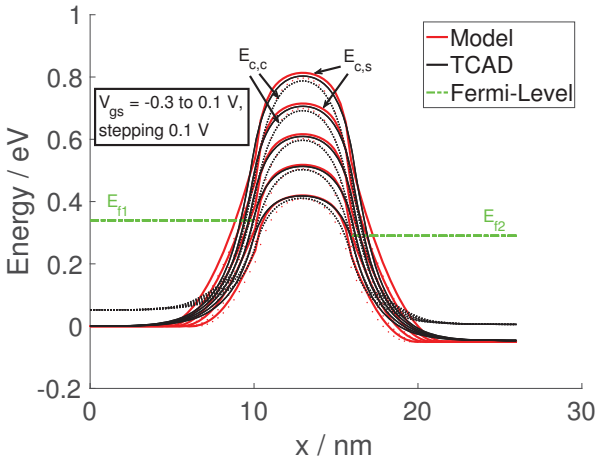

(a) Surface $E_{c,s}$ and center $E_{c,c}$ conduction band profile of the compact model compared with TCAD. The solid lines show the surface conduction band $E_{c,s}$ whereas the dashed lines show the center conduction band $E_{c,c}$.

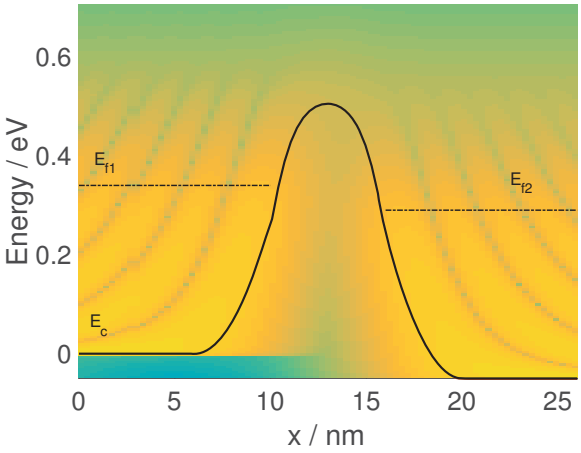

(b) Electron density with conduction band and both Fermi levels for an applied gate bias of $V_g = 0\,\mathrm{V}$.

Figure 6. Examination of the conduction band profile for a channel geometry of $l_{ch} = 6\,\mathrm{nm}$ and $t_{ch} = 2\,\mathrm{nm}$ at $T = 300\,\mathrm{K}$ and an applied drain bias of $V_{ds} = 0.05\,\mathrm{V}$.

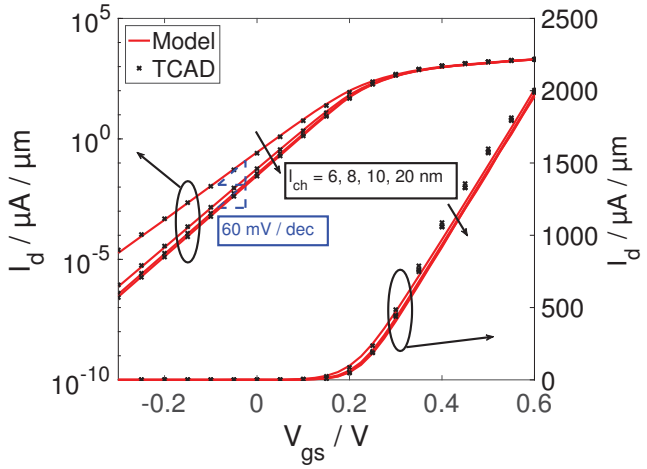

(a) Device with a channel thickness of $t_{ch} = 2\,\mathrm{nm}$.

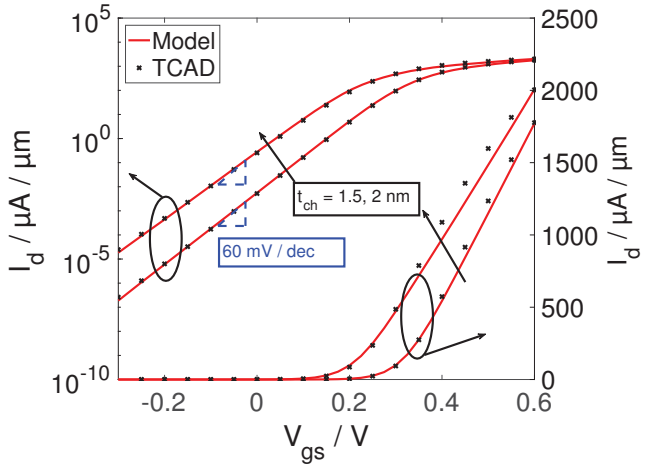

(b) Device with a channel length of $l_{ch} = 6\mathrm{nm}$.

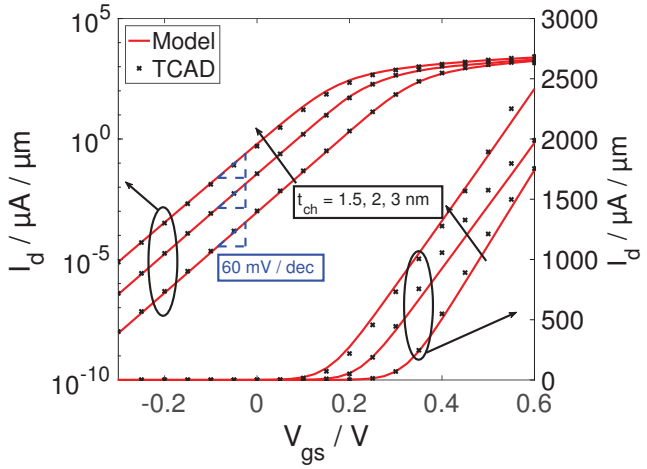

(c) Device with a channel length of $l_{ch} = 10\mathrm{nm}$.

Figure 7. Ballistic drain current per gate width of the transfer characteristic for a drain voltage of $V_{ds} = 0.05\,\mathrm{V}$ at $T = 300\,\mathrm{K}$.

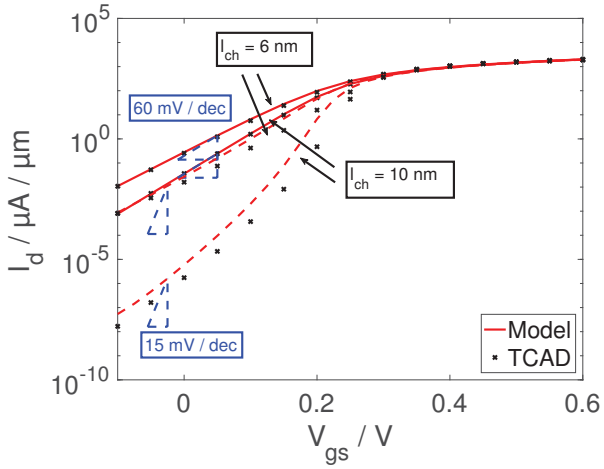

Figure 8. Ballistic drain current characteristic for channel geometry of $l_{ch} = 6,\ 10\,\mathrm{nm}$, $t_{ch} = 2\,\mathrm{nm}$ and a drain bias of $V_{ds} = 0.05\,\mathrm{V}$ at $T = 75\,\mathrm{K}$ (dashed lines) and at 300 K (solid lines). The triangle, showing a slope of 15 (60) mV/ dec denotes the ideal slope which could be reached for an pure thermionic emission current at $T = 75\,(300)\,\mathrm{K}$.

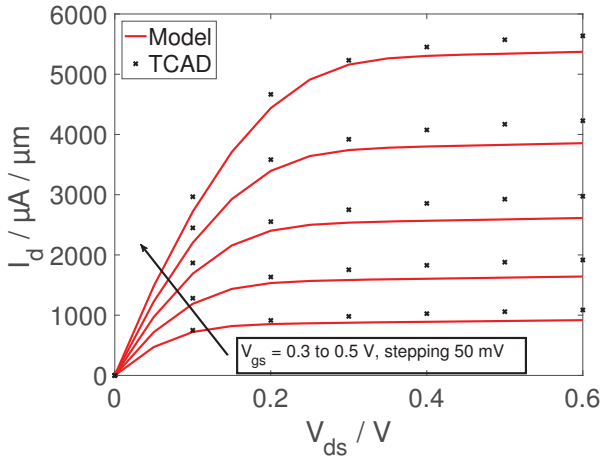

(a) Device with a channel length of $l_{ch} = 6\,\mathrm{nm}$.

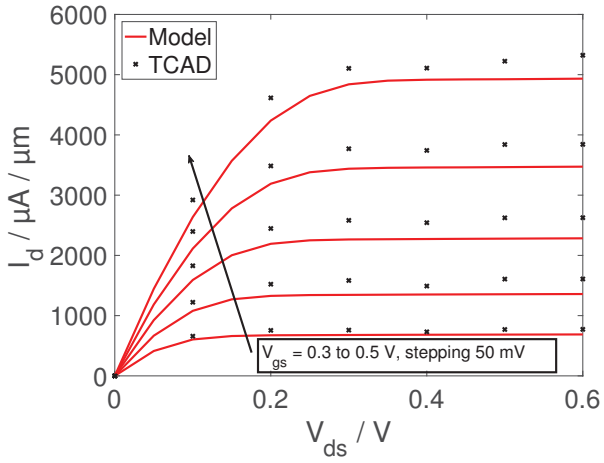

(b) Device with a channel length of $l_{ch} = 10\,\mathrm{nm}$.

Figure 9. Ballistic output current characteristic of the DG MOSFET, for a channel geometry of $t_{ch} = 2\,\mathrm{nm}$ at $T = 300\,\mathrm{K}$.

ACKNOWLEDGMENTS

This work is supported by the German Federal Ministry of Education and Research under contract No.03FH001I3. We would like to thank Keysight Technologies for the license donation of the software IC-CAP and AdMOS GmbH for support.

REFERENCES

[1] Z. Ren, S. Goasguen, A. Matsudaira, S. S. Ahmed, K. Cantley, Y. Liu, Y. Gao, X. Wang, and M. Lundstrom, "NanoMOS." https://nanohub.org/resources/1305, Mar 2016.
[2] J. Wang and M. Lundstrom, "Does Source-to-Drain Tunneling Limit the Ultimate Scaling of MOSFETs?." in *International Electron Devices Meeting IEDM*, pp. 707–710, Dec. 2002.
[3] Q. Rafhay, R. Clerc, G. Ghibaudo, and G. Pananakakis, "Impact of Source-to-Drain Tunnelling on the Scalability of Arbitrary Oriented Alternative Channel Material nMOSFETs." *Solid-State Electronics*, vol. 52, no. 10, pp. 1474 – 1481, 2008.
[4] J. Watling, A. Brown, A. Asenov, A. Svizhenko, and M. Anantram, "Simulation of Direct Source-to-Drain Tunnelling Using the Density Gradient Formalism: Non-Equilibrium Greens Function Calibration." in *International Conference on Simulation of Semiconductor Processes and Devices SISPAD*, pp. 267–270, 2002.
[5] S. Datta, "Nanoscale Device Modeling: the Green's Function Method." *Superlattices and Microstructures*, vol. 28, no. 4, pp. 253 – 278, 2000.
[6] G. Fiori and G. Iannaccone, "NanoTCAD ViDES." https://nanohub.org/resources/5116, Sep 2014.
[7] O. Baumgartner and Z. S. et al., *VSP-a Quantum-Electronic Simulation Framework*, pp. 701–721. Springer Science+Business Media, 2013.
[8] M. P. Anantram, S. S. Ahmed, A. Svizhenko, D. Kearney, and G. Klimeck, "NanoFET." https://nanohub.org/resources/1090, Mar 2016.
[9] F. Hosenfeld, M. Graef, F. Horst, A. Kloes, B. Iniguez, and F. Lime, "Modeling Approach for Rapid NEGF-Based Simulation of Ballistic Current in Ultra-Short DG MOSFETs." in *Mixed Design of Integrated Circuits and Systems MIXDES - 23rd International Conference*, pp. 52–57, June 2016.
[10] M. Graef, T. Holtij, F. Hain, A. Kloes, and B. Iniguez, "Improved Analytical Potential Modeling in Double-Gate Tunnel-FETs." in *Mixed Design of Integrated Circuits Systems (MIXDES)*, pp. 49–53, June 2014.
[11] A. Kloes, M. Schwarz, T. Holtij, and A. Navas, "Quantum Confinement and Volume Inversion in MOS3 Model for Short-Channel Tri-Gate MOSFETs." *IEEE Transactions on Electron Devices*, vol. 60, pp. 2691–2694, Aug 2013.
[12] M. Schwarz, T. Holtij, A. Kloes, and B. Iniguez, "Analytical Compact Modeling Framework for the 2D Electrostatics in Lightly Doped Double-Gate MOSFETs." *Solid-State Electronics*, vol. 69, pp. 72 – 84, 2012.
[13] E. Weber, *Electromagnetic Fields, Vol.I., Mapping of Fields*. John Wiley, New York, 1950.
[14] J. Wang, A. Rahman, A. Ghosh, G. Klimeck, and M. Lundstrom, "On the Validity of the Parabolic Effective-Mass Approximation for the I-V Calculation of Silicon Nanowire Transistors." *IEEE Transactions on Electron Devices*, vol. 52, pp. 1589–1595, July 2005.
[15] D. Selim, S. Gamal, W. Fikry, and O. A.-E. Halim, "Rapid and Efficient Method for Numerical Quantum Mechanical Simulation of Gate-All-Around Nanowire Transistors." in *International Conference on Microelectronics*, pp. 229–232, May 2012.
[16] S. Datta, "MATLAB codes from: Nanoscale device modeling: the Green's function method." https://nanohub.org/resources/19564, Oct 2013.
[17] E. N. Economou, *Green's Functions in Quantum Physics*. Springer Science+BusinessMedia, 2006.
[18] S. Datta, *Quantum Transport: Atom to Transistor*. Cambridge, 2005.
[19] S. Datta, *Electronic Transport in Mesoscopic Systems*. Cambridge University Press, 1997.
[20] R. Kim and M. Lundstrom, "Notes on Fermi-Dirac Integrals (3rd Edition)." Sep 2008.

Fabian Hosenfeld received the Bachelor and Master degree in electronic engineering from the Technische Hochschule Mittelhessen (THM) in Friedberg, Germany, 2013 and 2014, respectively. Currently he is working towards his PhD degree at the University Rovira i Virgili, Tarragona, Spain in cooperation with the THM, Giessen. Since 2013 he is working as a research assistant with the Research Group Nanoelectronics / Device Modeling at the Competence Center for Nanotechnology and Photonics, THM, Giessen, Germany.

Fabian Horst recieved the Bachelor and Master degree in electronic engineering from the Technische Hochschule Mittelhessen (THM) in Giessen, Germany in 2014 and 2015, respectively. Currently he is working towards his PhD degree at the University Rovira i Virgili, Tarragona, Spain in cooperation with the THM, Giessen. Since 2014 he is working as a research assistant with the Research Group Nanoelectronics / Device Modeling at the Competence Center for Nanotechnology and Photonics, THM, Giessen, Germany.

Michael Graef is currently pursuing the Ph.D. degree in electrical engineering from the Universitat Rovira i Virgili, Tarragona, Spain. He has been a Research Assistant with the Research Group Nanoelectronics/Device Modeling, Competence Center for Nanotechnology and Photonics, Technische Hochschule Mittelhessen, Giessen, Germany, since 2012.

Atieh Farokhnejad received the Bachelor degree in Electronic Engineering from Dr. Shariaty Technical University of Tehran, Iran, in 2012. Since 2015, she holds the M.Sc. degree in Information and Communications issued by Technische Hochschule Mittelhessen (THM) in Friedberg, Germany. Currently she is working towards her PhD degree at the University Rovira i Virgili, Tarragona, Spain in cooperation with the THM, Giessen.

Alexander Kloes (M'95) received the Diploma and Ph.D. degrees in electrical engineering from the Solid-State Electronics Laboratory, Technical University of Darmstadt, Darmstadt, Germany, in 1993 and 1996, respectively. He has been a Professor with Technische Hochschule Mittelhessen, Giessen, Germany since 2002.

Benjamín Iñíguez received the B.S., M.S., and Ph.D. degrees in physics from the University of the Balearic Islands, Balearic Islands, Spain, in 1989, 1992, and 1996, respectively. He joined the Universitat Rovira i Virgili, Tarragona, Spain, as Titular Professor in 2001, and he became a Full Professor in 2010. He obtained the ICREA Academia Award (ICREA Institute, Catalonia) in 2009 and 2014.

François Lime received the M.S. and Ph.D. degrees from the Institut National Polytechnique de Grenoble, Grenoble, France, in 2000 and 2004, respectively. He joined the Universitat Rovira i Virgili, Tarragona, Spain, as a Ramon y Cajal Researcher, in 2009, where he has been an Associate Professor since 2014. His current research interests are compact modelling of multiple-gate MOSFETs and OTFTs and the electrical characterization of these devices.